INORGANIC CHEMISTRY FRONTIERS

RESEARCH ARTICLE

View Article Online
View Journal | View Issue

Cite this: *Inorg. Chem. Front.*, 2024, **11**, 6536

Long-wavelength near-infrared emission in chromium-activated $LiZnNbO_4$ spinel crystals and valence-converting enhancement *via* Er^{3+} ion heterotopic doping†

Wen Song,[a] Kaiwen Zhang,[a] Xiaoyi Dong,[a] Liang Xu,[a] Yongjin Li, *[a,b] Rui Hu,*[c] Zhaoyi Yin,[a,b] Zhengwen Yang,[a,b] Jianbei Qiu [a,b] and Zhiguo Song *[a,b]

Realizing efficient long-wavelength near-infrared (NIR) emission of Cr^{3+} ions is still a challenge in spinel-based phosphors due to the limitations of strong crystal fields. Here, we propose three design strategies for obtaining weak crystal fields in spinel-type crystals, and report for the first time designed Cr-activated $LiZnNbO_4$ (LZNO) crystals with unique weak crystal fields and application of an NIR enhancement strategy *via* heterotopic and heterovalent doping with trivalent rare earth ions. Under irradiation with 468 nm blue light, the phosphor presents ultra-wideband NIR emission centered at 800 nm covering the region of 650–1300 nm, which is attributed to the larger radius, high valence state of cations and the low symmetry of octahedral sites in the LZNO spinel. Supported by XRD refinement, XPS analysis, and density functional theory (DFT) calculation results, it was shown that when Er^{3+} ions are designedly doped with the Zn^{2+} sites of the spinel crystals, effective promotion of the valence state transformation of Cr^{4+} to Cr^{3+} in the LZNO:Cr^{3+} system is achieved by defect charge compensation, and this enhances the NIR emission by nearly 3 times. The results of this work not only enrich the material family of Cr^{3+}-activated NIR emitting phosphors, but also offer a novel and simple method for improving the luminescence efficiency of Cr^{3+}-activated phosphors.

Received 10th May 2024,
Accepted 3rd August 2024

DOI: 10.1039/d4qi01168f

rsc.li/frontiers-inorganic

1 Introduction

NIR light sources have received increasing attention due to their wide range of applications in night vision, plant growth, biosensing, quantitative composition analysis and nondestructive testing.[1–4] In recent years, the emergence of NIR-emitting phosphor-converted light-emitting diodes (NIR pc-LEDs) has greatly expanded the development and utilization of NIR technology in practical applications due to their low cost, long lifespan, miniaturization, highly efficient luminosity and fast response characteristics.[5,6] The key to the production of efficient NIR pc-LEDs is the preparation of NIR luminescent phosphors that can be effectively pumped by blue light. Therefore, researchers have made significant efforts to explore a large number of NIR inorganic luminescent phosphors doped with active ions, including transition metal ions (*e.g.*, Cr^{3+}, Cr^{4+}, Fe^{3+}, Ni^{2+}, and Mn^{4+}), Bi^{2+} ions and lanthanide ions (*e.g.*, Pr^{3+}, Nd^{3+}, Eu^{2+}, Tm^{3+}, Yb^{3+} and Er^{3+}).[7–13] Among them, the transition metal ion Cr^{3+} can demonstrate broad absorption capacity that is well-aligned with blue LED chips and it can emit photons ranging from 650 to 1300 nm when located in a weak octahedral crystal field.[14–17] This enhances its potential for use in the creation of NIR light source devices, addressing the crucial issue of emerging phosphorus powder-coated NIR pc-LEDs. However, just like every coin has two sides, long-wavelength emission is frequently associated with low luminous efficiency. Many reported Cr^{3+} phosphors still exhibit low photoluminescence efficiency and insufficient full width at half maximum (FWHM). This greatly hinders the practical application development of NIR pc-LEDs.[18–20] Therefore, research work on developing new Cr^{3+}-activated materials, as well as methods that can effectively improve their luminescence efficiency, are still urgently needed.

Spinel materials are considered as excellent hosts for photoluminescence because of their ability to adjust crystal structures and their suitability for ion doping.[21] However, most of the octahedral sites of spinel phosphors typically exhibit strong crystal fields, leading to the emission of the doped Cr^{3+} ion being located at about 700 nm (several Cr^{3+}-activated

[a]*Faculty of Materials Science and Engineering, Kunming University of Science and Technology, Kunming 650093, PR China. E-mail: liyongjin@kust.edu.cn, songzg@kmust.edu.cn*
[b]*Key Lab. of Advanced Materials of Yunnan Province, Kunming 650093, PR China*
[c]*Collage of Chemistry and Chemical Engineering, China West Normal University, Nanchong 637000, PR China. E-mail: hr2022@cwnu.edu.cn*

† Electronic supplementary information (ESI) available. See DOI: https://doi.org/10.1039/d4qi01168f

spinel-type NIR phosphors are listed in Table S1†).[22] This NIR emission property greatly limits the practical application of spinel phosphors in some scenarios like food analysis[23,24] and biological imaging.[25] However, until now, from the perspective of materials selection and design, there is little understanding of obtaining long-wavelength broadband NIR in Cr^{3+}-activated spinel phosphors.

The long wavelength emission of Cr^{3+} ions in octahedral sites is most likely due to weak crystal fields. This phenomenon is frequently observed in Cr^{3+}-doped garnet-structured phosphors featuring local low-symmetry unit cells.[26–29] On the basis of these findings, we recognize that this feature is possibly applicable in achieving Cr ion long-wavelength broadband emission in spinel phorhpors. Based on controlling the redshift of Cr ion emission wavelength in garnets, we propose the following design principles for achieving Cr ion long-wavelength broadband emission: 1. (high valence state) the higher the valence state of the cation, the larger the volume of its coordination polyhedron, which can weaken the crystal field around Cr; 2. (large radius) the larger radius of the cation always corresponds with longer bond lengths and greater metal–ligand distances, which can decrease the crystal field; and 3. (low symmetry) the large spatial structure and low symmetry are more likely to cause polyhedral distortion, thereby causing uneven distribution of electric fields and intensifying the splitting of Cr^{3+} sub-energy levels.

According to the above given criteria, we initially considered designing phosphors with niobate materials, as they contain Nb^{5+} ions with high valence and larger ionic radius. Then the $LiZnNbO_4$ compound was selected because it can manifest the behavior of a superstructure or existence of empty interstitial space.[30] This feature can easily result in local distortion in the doping process, as well as low local symmetry. In addition, it is also expected to provide suitable octahedral sites for Cr^{3+}. Therefore, these structural characteristics indicate that the compound has significant potential for producing long-wavelength broadband NIR emission activated by Cr^{3+}.

On the other hand, it is important to mention the dominant factor that affects the luminescence of Cr^{3+}-doped phosphors. It is common in the high-temperature synthesis of phosphors that the self-oxidation process of Cr^{3+}-doped materials sintered in air will, in general, partially form Cr^{4+} ions.[31] Due to the low and unsatisfactory actual formation rate of Cr^{3+}, a significant amount of luminescence "killer" Cr^{4+} with intense absorption in the NIR region can function as a non-radiative relaxation center, capturing energy and significantly impacting the luminescence efficiency of the phosphor.[32] Although it can be partially prevented by the reducing atmosphere, this method is not suitable for all hosts. As a result, to address the issue of the low luminescence efficiency of Cr^{3+} due to these mentioned factors, researchers have carried out thorough research and suggested several effective methods. One uses energy transfer[33–35] of suitable sensitizers, such as Er^{3+} ions, to boost their luminescence effectiveness. However, due to the limitation of forbidden f–f transitions, the enhancement effect of rare earth ions is still far from satisfactory in practical applications. Therefore, exploring a suitable method that can inhibit the generation of Cr^{4+} simply and effectively will provide new insight into studying Cr^{3+}-activated NIR phosphors.

In this work, to address the challenges associated with exploiting new Cr^{3+}-activated spinel materials with long-wavelength NIR emission while devising a novel strategy to improve the luminescence efficiency, we exploited the NIR emission of a Cr-doped $LiZnNbO_4$ spinel system, as well as enhancing the formation of Cr^{3+} ions by heterotopic charge compensation of Er^{3+} ions for the first time. Based on optical and structural analyses and DFT calculations, it is shown that the octahedral sites of the LZNO spinel exhibit special weak crystal fields, and Cr^{3+}-ion dopants present NIR emission centered at 800 nm as supposed. Moreover, when the Er^{3+} ion is selected for designed heterotopic doping at the Zn^{2+} site, Cr^{4+} luminescence assassins, which occupy the octahedral sites of Nb^{5+} ions, are transformed into beneficial Cr^{3+} emission centers by defect charge compensation. The universality experiments indicated that the strategy of heterotopic and heterovalent doping of trivalent rare earth ions offers a simple but efficient way to enhance the NIR luminescence efficiency of Cr^{3+} phosphors. Finally, under the excitation of a 470 nm blue laser, the quantum efficiency of $LiZn(Er)NbO_4:Cr^{3+}$ is enhanced from 8.3% to 17.6%. The use of pc-LEDs in combination with commercial blue-light chips demonstrated significant potential in biological organ imaging and night-vision applications.

2 Experimental section

2.1 Materials and preparation

Powder samples containing $LZNO:xCr^{3+}$ (x = 0–0.03) and $LiZn_{1-y}(Er)_yNbO_4:0.01Cr^{3+}$ (y = 0–0.02) compositions were synthesized by high-temperature solid-phase reactions. Raw materials of Li_2CO_3 (99.9%), ZnO (99.99%), Nb_2O_5 (99.99%), Cr_2O_3 (99.99%) and Er_2O_3 (99.99%) were weighed stoichiometrically (all raw materials are purchased from Aladdin reagents, https://www.aladdinsci.com), mixed and ground in an agate mortar for at least 30 min to create a well-homogenized powder. Then, the mixture was placed into an alumina crucible and sintered under an air atmosphere at 1100 °C for 4 h until it naturally cooled to room temperature. After cooling to room temperature naturally, the samples were ground into powders, which are the final target phosphors for further measurements. NIR pc-LEDs were fabricated using the optimal composition of $LiZn_{0.986}Er_{0.014}NbO_4:0.01Cr^{3+}$ (λ_{em} = 800 nm) with high-power blue-LED chips (5 W, 470 nm, San'an Optoelectronics Co., Ltd). The phosphor was evenly mixed with epoxy resin in a weight ratio of 1 : 1 and then applied to the chips.

2.2 Characterization

X-ray diffraction (XRD) patterns were obtained using a Bruker D8 X-ray diffractometer with Cu Kα radiation (λ = 1.54056 Å) at 40 kV and 40 mA. The general structure analysis system (GSAS) program was used to perform the Rietveld refinements of XRD

profiles. The morphological properties were characterized using a scanning electron microscope (SEM, SU8000, Hitachi) equipped with an energy dispersive X-ray spectroscopy (EDS) system. A UV-3600 spectrometer was utilized for recording the diffuse reflectance (DR) spectra. Photoluminescence spectra at room temperature (RT) and different temperatures were recorded using an FLS-980 spectrometer. The NIR photoluminescence quantum yield (PLQY) values were measured using a Quantaurus-QY Plus instrument (C13534-12, Hamamatsu Photonics) and the luminescence decay time was measured using an integrated sphere on an Edinburgh FLS1000 spectrophotometer. X-ray photoelectron spectra (XPS) were recorded using an ESCALAB 250 photoelectron spectrometer (ThermoFisher Scientific, USA) with Al Kα (1486.6 eV) as the X-ray source. Electroluminescence (EL) spectra and the performances of the fabricated NIR pc-LED devices were measured using an integrating sphere (Labsphere) and the data were collected using a high accuracy array spectroradiometer (HAAS-2000, Everfine). Visible images and NIR images were obtained using a modified visible/infrared camera (Canon M100).

2.3 Calculation details

The crystal structures of LZNO, LZNO-Cr and LZNO-Cr-Er were optimized using the Vienna *ab initio* simulation package, which is a plane-wave pseudopotential total energy package based on density functional theory (DFT).[36] The atomic positions and cell parameters were relaxed with an electronic convergence criterion of 1×10^{-5} eV and an atomic convergence criterion of 0.01 eV $Å^{-1}$. A cutoff energy of 520 eV was used for the basis set of plane waves and a $2 \times 2 \times 1$ *Γ*-centered Monkhorst–Pack *k*-point grid was used to sample the first Brillouin zone. The Perdew–Burke–Ernzerhof (PBE) exchange–correlation functional was employed for structural optimization, density of states and charge density calculations, whereas the subsequent electronic properties were determined using the HSE06 hybrid functional.[37]

3 Results and discussion

3.1 Phase, crystal structure and morphology

Fig. 1a shows the components of LZNO where it adopts a non-centrosymmetric tetragonal crystal structure with the $P4_122$ space group. Usually, asymmetric crystals can result in an uneven distribution of electric fields, which leads to smaller crystal fields.[38] In addition, the structure comprises two crystallographically independent octahedral units, LiO_6 and NbO_6, which are linked through shared edges and angles. The ZnO_4 tetrahedra are linked to two octahedra only through shared angles, resulting in a large spatial gap. The Li–O and Nb–O bond lengths in the two octahedra are 2.173 and 2.016 Å, respectively, indicating a greater distance between the metal and the ligand. On the other hand, as the radius of Cr^{3+} (CN = 6, r = 0.615 Å) is closer to that of Nb^{5+} (CN = 6, r = 0.64 Å), when the Cr^{3+} ion is doped with LZNO, it is easier to enter the Nb^{5+} position with octahedral coordination as a luminescent center. Therefore, the analysis results indicated that the LZNO crystal structure is in line with our proposed three criteria, namely 1. high valence state, 2. large radius, and 3. low symmetry.

Fig. 1b shows the diffraction profiles of all the samples and they agree with those of the tetragonal spinel $LiZnNbO_4$ phase [ICDD no. 23-1206], indicating that the high-purity target product was successfully prepared. The card number was matched using Jade software. Additionally, it should be noted that a previous article reported the ICSD number of the $LiZnNbO_4$ compound as 85735.[39] To further determine the target phase and crystal structure, the XRD data were analyzed by adopting the Rietveld refinement, as shown in Fig. 2. The confidence factors R_{wp} and χ^2 are shown in Table S3† and they indicate reliable refinement results for all the samples. The obtained data indicate good phase purity of the synthesized products and yield their structural parameters.

The SEM images of the two representative LZNO:1%Cr^{3+} and LZNO:1%Cr^{3+},1.4%Er^{3+} samples are displayed in Fig. 1c and d. Both samples exhibit good crystallinity and a dense microstructure. It can be seen that the samples contain individual irregular block structures with smooth surfaces, and the particle size is in the range of 20–30 μm. Co-doping with Er^{3+} did not cause significant morphological changes. Moreover, the EDS mapping of the LZNO:1%Cr^{3+},1.4%Er^{3+} sample was also conducted on a randomly selected plate, as shown in Fig. 1e. This further proves the homogeneous distribution of constituent elements in the grain. Notably, the Li element was ionized by the electron beam in the chamber and could not be observed in the EDS mapping spectrum due to the experimental limitations.

3.2 Site occupation and theoretical calculations

In order to clearly determine the site occupancy of Cr ions in the LZNO crystals, the refined cell parameters with increasing doping concentration of Cr^{3+} are plotted, as shown in Fig. 2f. This shows that parameters a, b, c and V initially increase and then decrease, as the concentration of Cr^{3+} increases. This non-linear trend indicates that Cr ions have successively occupied different sites. As is well known, Cr^{3+} prefers to occupy the octahedrally coordinated environment due to its luminescence nature. Therefore, the luminescence properties of Cr^{3+} are typically observed and discussed in the context of a six-coordinated environment, specifically the octahedral site.[40] Considering the crystal structure of LZNO containing two crystallographically independent octahedral sites (NbO_6 and LiO_6 octahedra), it is meaningful to determine the site occupation preference of Cr^{3+}. As stated above, the radius of Cr^{3+} is closer to that of Nb^{5+}, and it is easier to enter the Nb^{5+} sites with octahedral coordination. Nevertheless, taking into account that the substitution of Nb^{5+} with Cr^{3+} will result in an excess of free electrons, it probably leads to the formation of defects and charge imbalance. Thus, the Cr^{3+} ion can easily be oxidized into the higher valence state of Cr^{4+} (CN = 6, r = 0.55 Å). This is because that when Cr^{4+} replaces Nb^{5+}, it is beneficial

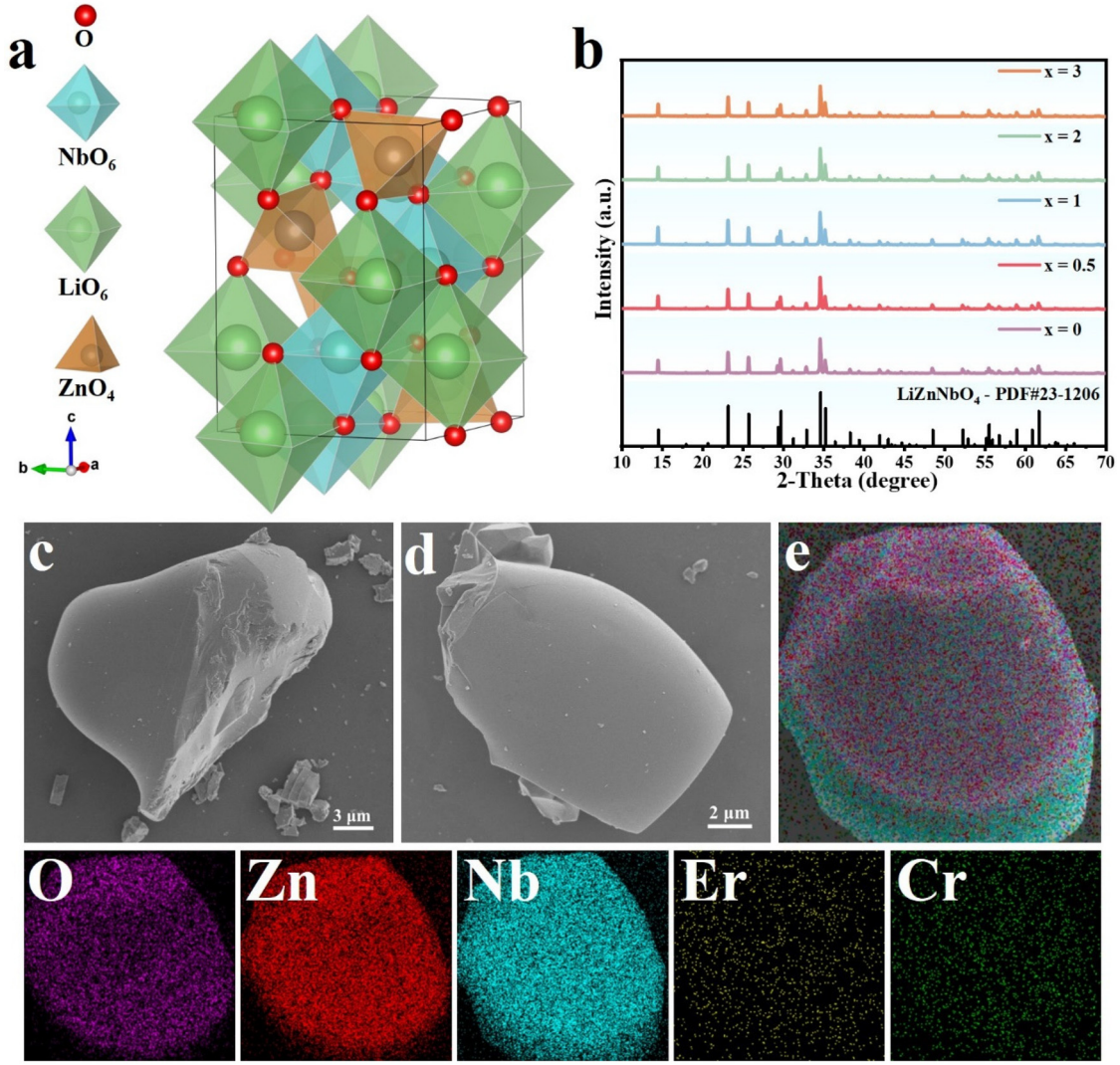

Fig. 1 (a) Crystal structure schematic illustration of LZNO. (b) XRD patterns of LZNO:x%Cr^{3+} (x = 0, 0.5, 1, 2 and 3) at room temperature. SEM images of (c) LZNO:0.01Cr^{3+} and (d) LZNO:0.01Cr^{3+},0.014%Er^{3+}. (e) EDS mapping of LZNO:0.01Cr^{3+},0.014%Er^{3+}.

for maintaining the stability of the system towards charge balance.

According to the above analysis and taking into account the characteristic emission of Cr^{3+} in the PL spectrum (Fig. 3a and b), we can consider that, at a low Cr^{3+} doping level, Cr^{3+} primarily replaces Zn^{2+} (CN = 4, r = 0.6 Å), and any remaining Cr^{3+} will enter the Nb^{5+} site simultaneously to maintain the electrical neutrality of the system. Then, as the Cr-doping content increases, it becomes easier to form Cr^{4+} to stably exist at Nb^{5+} sites while maintaining the system's electrical neutrality. Undoubtedly, replacing Nb^{5+} with Cr^{4+} will cause lattice contraction, resulting in a decrease in cell parameters. Therefore, although we only considered replacing Nb^{5+} with $Cr^{3+}/^{4+}$ from the initial experimental observation, we believe that in the actual synthesis process, there is a portion of Cr^{3+} ions that will actively replace the Zn^{2+} ions to maintain a certain charge balance. This could result in a reduction in the creation of efficient luminescent sites. As is well known, the electronic structure of host materials is closely related to the luminescence performance of phosphors. However, the electronic structure of LZNO has never been reported in previous studies. Therefore, to better understand LZNO crystals, their electronic structure was calculated and analyzed using the DFT method and VASP software. The detailed information and descriptions are presented in the ESI (Fig. S1 and S2†).

3.3 Photoluminescence

The DR spectra of LZNO:x%Cr^{3+} (x = 0.5, 1, 2 and 3) were recorded as shown in Fig. 3a. The absorption spectrum of the undoped sample is consistent with the calculated electronic structure of LZNO crystals (Fig. S2†). This indicates an indirect bandgap with allowed transitions, which results in an optical bandgap of 2.81 eV. The Cr^{3+}-substituted samples exhibit intense absorption at around 463 and 653 nm in the DR spectrum, corresponding to the $^4A_2 \rightarrow {}^4T_1$ (4F) and $^4A_2 \rightarrow {}^4T_2$ (4F) Cr^{3+} electronic transitions, respectively. The optical bandgap

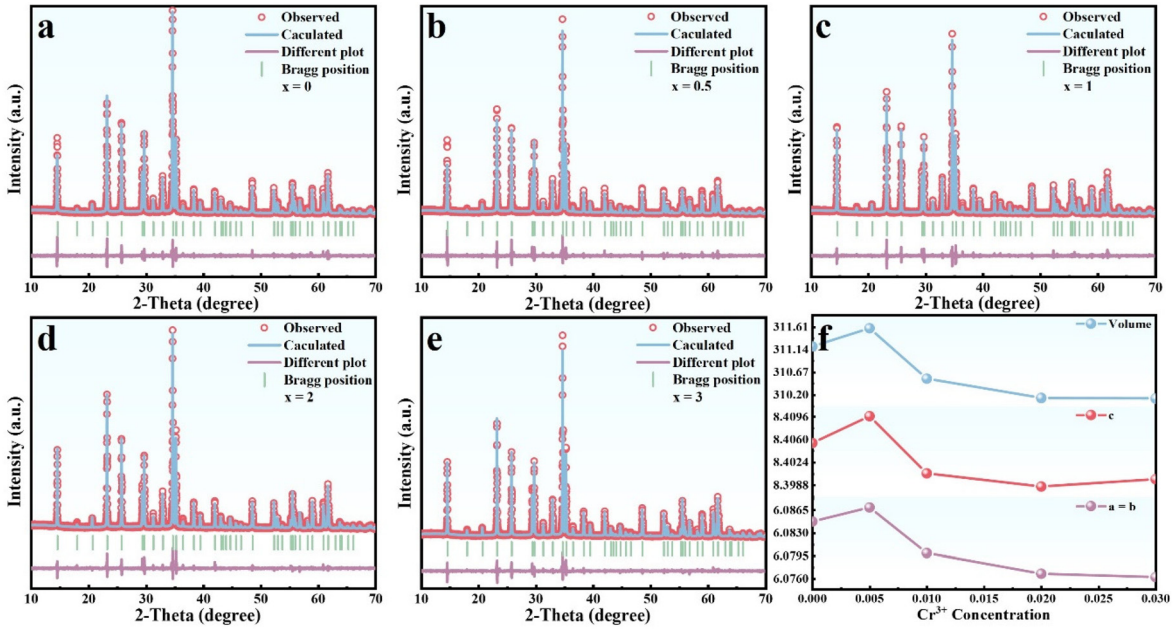

Fig. 2 Rietveld refinement of LZNO:*x*%Cr^{3+} with (a) x = 0, (b) x = 0.5, (c) x = 1, (d) x = 2, and (e) x = 3. (f) Changes in the cell parameters (*a*, *b*, and *c*) and unit cell volume in LZNO:*x*%Cr^{3+} with increasing x.

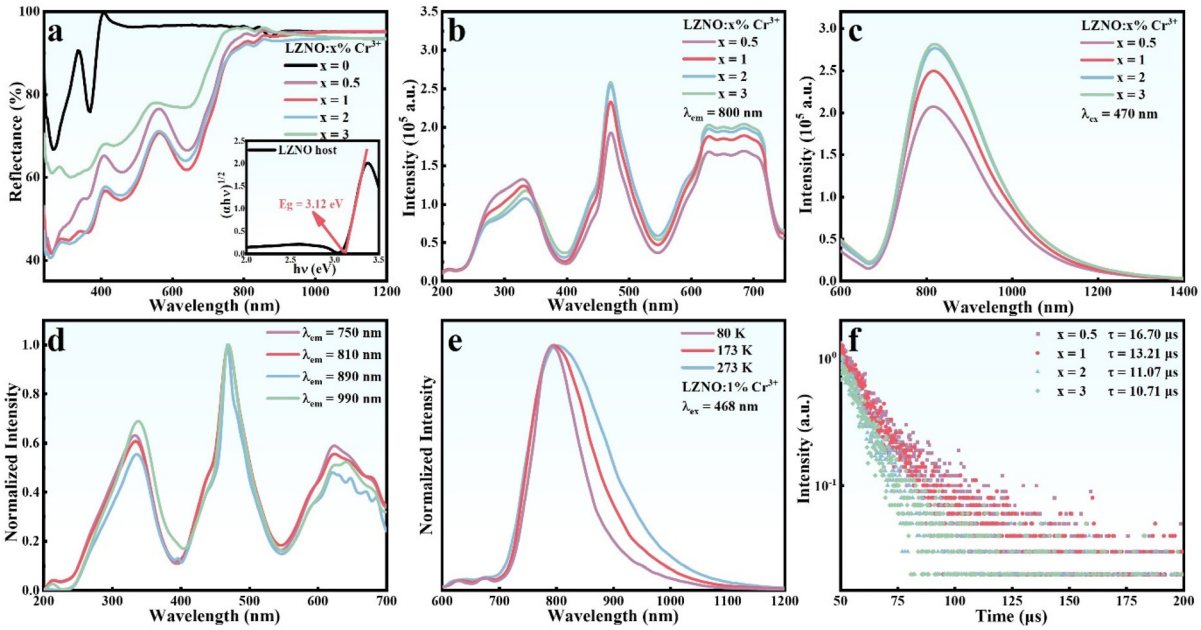

Fig. 3 (a) DR spectra of LZNO:*x*%Cr^{3+} (x = 0, 0.5, 1, 2 and 3); the inset is an absorption spectrum of LZNO calculated using the Kubelka–Munk equation. (b) PLE and (c) PL spectra of LZNO:*x*%Cr^{3+} (x = 0, 0.5, 1, 2 and 3). (d) Excitation spectra of LZNO:*x*%Cr^{3+} at different monitoring wavelengths. (e) Emission spectra of LZNO:0.01Cr^{3+} measured at 273, 173 and 80 K. (f) PL decay curves of LZNO:*x*%Cr^{3+} (x = 0, 0.5, 1, 2 and 3) monitored at 800 nm.

(E_g) of LZNO can be evaluated by fitting the data with eqn (1):[41,42]

$$[h\nu\alpha]^{1/n} = A(h\nu - E_g) \quad (1)$$

where $h\nu$, α, E_g, and A refer to the photon energy, absorption coefficient, bandgap, and proportionality constant, respectively. The value of the exponent n is determined by the properties of electronic transition. The n values for the direct allowed transition, direct forbidden transition, indirect

allowed transition, and indirect forbidden transition are 1/2, 3/2, 2 and 3, respectively.[43–45] The obtained bandgap of 3.12 eV (Fig. 3a) is in good agreement with our theoretical calculations. Fig. S3a† shows the band gap changes of LZNO after doping it with different concentrations of Cr^{3+}. It can be clearly seen that as the Cr^{3+} doping concentration increases from 0.5% to 3%, the band gap of LZNO gradually decreases from 3.08 eV to 2.33 eV. According to Fig. S1,† Cr^{3+} doping will form impurity energy levels near the top of the valence band of the LZNO host, leading to a gradual decrease in the bandgap width.

Significantly, we did not detect any distinctive absorption peaks associated with Cr^{4+}, as mentioned earlier. This is an intriguing phenomenon, as Cr^{4+} seems to be playing a game of "hide and seek" with us. To coax out this "naughty mouse," we conducted tests on the DR spectrum of LZNO highly doped with Cr^{3+} (Fig. S3†). When the Cr^{3+} doping concentration reaches or exceeds 4%, a new absorption peak emerges at 575 nm, unmistakably associated with the characteristic $^3A_2 \rightarrow {}^3T_1$ (^3F) absorption transition of Cr^{4+}.[46] Cr^{4+} typically undergoes specific energy level transitions only in a tetrahedral coordination environment, whereas the Cr^{4+} in LZNO remains stable in an NbO_6 octahedral coordination environment, making it undetectable. As the doping level of Cr^{3+} increases, a larger amount of Cr^{4+} is more readily produced in the system. Consequently, to maintain charge balance, Cr^{4+} will actively occupy the ZnO_4 tetrahedral site, leaving it with no means of escape.

Then, to verify Cr^{3+} as the luminescent ion in the LZNO host, both the excitation spectra (Fig. 3b) and the emission spectra (Fig. 3c) of LZNO with Cr concentrations from 0.5% to 3% were investigated. The excitation spectrum covers a wide region of 250–750 nm, and the peaks centered at 325, 468 and 650 nm correspond to the $^4A_2 \rightarrow {}^4T_1$ (4P), $^4A_2 \rightarrow {}^4T_1$ (4F) and $^4A_2 \rightarrow {}^4T_2$ (4F) spin-allowed transitions of Cr^{3+} in a weak octahedral crystal field.[47,48] Under 468 nm excitation, the phosphor exhibits an ultra-broadband emission spectrum centered at 800 nm with an FWHM of about 200 nm, which is attributed to the spin-allowed $^4T_2 \rightarrow {}^4A_2$ (4F) transition of the octahedrally coordinated Cr^{3+} ions.[49] Concurrently, the emission intensity of Cr^{3+} is less affected by the doping concentration, which may also be related to the limited luminescence efficiency of Cr^{3+} owing to the increased content of non-emission Cr^{4+}.

In order to confirm whether the crystal field environment of Cr^{3+} in the LZNO host meets our standards as a weak field, we performed quantitative calculations. The crystal field strength can be characterized by crystal field splitting (D_q) and the Racah parameter (B) calculated using eqn (2)–(4):[50]

$$10D_q = E(^4T_2) = E(^4A_2 \rightarrow {}^4T_2) \quad (2)$$

$$\frac{D_q}{B} = \frac{15(x-8)}{x^2-10x} \quad (3)$$

$$x = \frac{E(^4A_2 \rightarrow {}^4T_1) - E(^4A_2 \rightarrow {}^4T_2)}{D_q} \quad (4)$$

The calculated D_q and B parameters equal to 1459.8 and 722.7 cm^{-1} yield a D_q/B ratio of 2.02 upon examination of the data. The corresponding Tanabe–Sugano energy level diagram of the Cr^{3+} ion in octahedral coordination is shown in Fig. S4.† This indicates that the [NbO_6] octahedra in the LZNO host indeed provide a relatively weak crystal field environment for Cr^{3+}. The principles we proposed in this work may offer practical solutions for designing long-wavelength broadband NIR emitting spinel materials and even other material systems activated by Cr^{3+} in weak crystal fields.

In addition, we observed that the Cr^{3+} emission peak in the LZNO host is asymmetric. Since the LiO_6 octahedral site is also suitable as a luminescent site for Cr^{3+}, it is necessary to analyze and determine the actual luminescent center of Cr^{3+}. The excitation spectra, which were normalized and monitored at different wavelengths (λ_{em} = 750, 810, 890, and 990 nm, Fig. 3d), show a significant overlap, clearly demonstrating that there are no multiple crystallographically independent emission sites. Meanwhile, the low-temperature-dependent spectrum of LZNO:1%Cr^{3+} is displayed in Fig. 3e. As the temperature gradually decreases, the emission peak undergoes a slight blue shift and becomes narrower, which is attributed to the reduced electroacoustic coupling between Cr^{3+} and the environment. However, no new emission peaks appeared, further indicating that the transition emission process of Cr^{3+} in the host is independent and singular with no multiple luminescent centers. Conversely, the asymmetric emission spectra may be attributed to local structural distortion around the Cr^{3+} cation, which exacerbates the low symmetry of the crystal field and results in uneven peak broadening.

Fig. 3f shows the RT photoluminescence decay curve of LZNO:Cr^{3+} obtained by exciting the phosphor at 468 nm while monitoring at 800 nm. All the decay curves can be accurately fitted by a single-exponential function. These findings further corroborate the dominance of a single type of emission center in this phosphor. As the concentration of Cr^{3+} increases from 0.5% to 3%, the decay curves exhibit a reduction in lifetime, dropping from 16.7 to 10.1 μs. This is due to the concentration quenching effect of Cr^{3+} and the combined effect of Cr^{4+} as the energy transfer center. Hence, in LZNO:1%Cr^{3+} under 468 nm excitation, the QY value is determined to be 8.3% (Fig. S5†) and it is relatively low. Therefore, it is imperative to suppress the generation of Cr^{4+} and stabilize the valence state of Cr^{3+}.

3.4 NIR enhancement by heterotopic doping of Er^{3+}

As we know, the luminescence properties of Cr^{3+}-activated phosphors will be suppressed because of the formation of Cr^{4+}, especially during inequivalent substitution of Cr^{3+} for Nb^{5+} in the doping process. Doping charge compensator ions into phosphors is a common method to improve inequivalent substitution. In order to avoid competition with Cr ions entering the LZNO host lattice, we designed charge compensation by doping rare earth ions of Er^{3+} at the Zn^{2+} sites. The XRD

patterns and Rietveld refinement results of co-doped Er^{3+} are shown in Fig. S6 and S7.† While maintaining purity, the trend of the overall expansion of crystal cell parameters indicates the successful replacement of Zn^{2+} by Er^{3+}. It should be noted that the radius difference between Er^{3+} (CN = 6, r = 0.89 Å) and Zn^{2+} (CN = 4, r = 0.6 Å) is significant, but this is a comparison under different coordination environments. We know that when Er^{3+} enters the four-coordinated Zn site, its radius will inevitably decrease due to the change in the coordination environment from six to four. This process will also force the Cr ions originally intended to enter the Zn^{2+} sites to enter the Nb^{5+} sites instead as potentially effective luminescent centers.

To confirm the role of heterotopic doping of Er^{3+} in the increase of Cr^{3+} ions, the DR spectra and NIR luminescence performances of 1%Cr doped samples with varying concentrations of Er^{3+} were investigated. The introduction of Er^{3+} significantly enhances the light absorption of Cr^{3+} ions, indicating that the content of Cr^{3+} in the system may be increased (Fig. 4a). The additional absorption peaks at 520, 970 and 1455–1640 nm are attributed to electronic transitions from the ground state $^4I_{15/2}$ of Er^{3+} to its $^2H_{11/2}$, $^4I_{11/2}$ and $^4I_{13/2}$ excited states, respectively. The PL and PLE spectra of the $Li_{1-x}Er_xZnNbO_4$:0.01Cr^{3+} samples are shown in Fig. 4b and c. The peak shapes of the PLE and PL spectra are similar to those of single-doped Cr^{3+}, and there is no significant positional deviation. As the doping concentration of Er^{3+} reaches 1.4%, the integrated intensity of the Cr^{3+} emission band (650–1300 nm) is 2.9 times that of the original sample. The subsequent decrease in intensity is attributed to concentration quenching. The IQE (17.6%) of the optimal 1.4%Er^{3+} co-doped sample is more than two times that compared to the sample doped solely with 1%Cr^{3+} (8.3%). We also noticed that as the concentration of Er^{3+} increases, a new concave peak appears at 808 nm in the PL spectrum. Fig. S9† shows the low-temperature-dependent spectrum of the 1.4%Er^{3+} co-doped sample, analyzing the reason for the formation of this concave peak. At lower temperatures, the concave peak becomes more noticeable. When Er^{3+} is in an excited state, there is a higher likelihood of reabsorbing the photons it emits, particularly at lower temperatures. Therefore, the concave peak at 808 nm is due to the self-absorption of the $^4I_{9/2}$ level of Er^{3+}. The decay curve of co-doped Er^{3+} is presented in Fig. 4d. Co-doping with Er^{3+} leads to a reduction in the lifetime of Cr^{3+}, suggesting that the localized defect energy level created by Er^{3+} at the bottom of the conduction band has a trapping effect for electrons.

Due to the significant substitution radius of Er^{3+}, it may lead to a modification in the rigidity of the crystal structure, subsequently impacting the near-infrared luminescence of Cr^{3+}. The fluorescence thermal stability, which can indirectly reflect the structural rigidity of $LiZn_{1-x}Er_xNbO_4$:0.01Cr^{3+} (x = 0 and 0.014), was examined through temperature-dependent emission spectra recorded from 298 to 473 K under 468 nm excitation, as shown in Fig. S10.† The 3D mapping surface for the emission spectrum of $LiZn_{99.86}Er_{0.014}NbO_4$:0.01$Cr^{3+}$ is plotted in Fig. 4e. When heated to 423 K, its integrated emission intensity remains at about 12% of the RT (298 K) value. Fig. 4f shows the temperature variation curves of LZNO:0.01Cr^{3+} and $LiZn_{0.986}Er_{0.014}NbO_4$:0.01$Cr^{3+}$ phosphors, indicating that Er^{3+} doping has almost no effect on the structural rigidity of LZNO crystals, and thus, the enhancement of

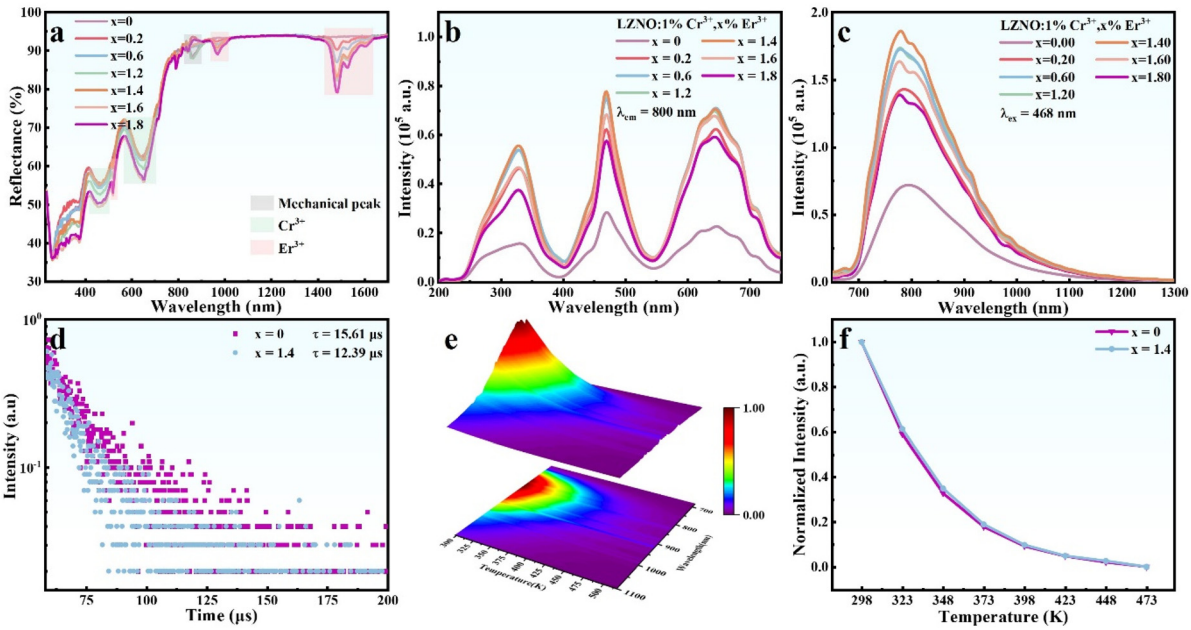

Fig. 4 (a) DR spectra of LZNO:1%Cr^{3+},x%Er^{3+} (x = 0–1.8). (b) PLE and (c) PL spectra of representative LZNO:1%Cr^{3+},x%Er^{3+} (x = 0–1.8). (d) PL decay curves of LZNO:0.01Cr^{3+} and LZNO:0.01Cr^{3+},0.014Er^{3+} monitored at 800 nm. (e) 3D mapping surface plot of the emission spectra of the LZNO:0.01Cr^{3+},0.014%Er^{3+} phosphor excited at 468 nm as a function of temperature. (f) Normalized integrated intensity of the emission spectra as a function of temperature.

Cr^{3+} luminescence is independent of crystal rigidity. More detailed analysis regarding the fluorescence thermal stability can be found in Fig. S11–S13 in the ESI.†

3.5 Underlying mechanism of NIR enhancement by trivalent rare earth ions

Spectral analysis and thermal stability studies have indicated that the increase in the NIR emission of Cr^{3+} in the LZNO system through co-doping with Er^{3+} is not attributed to energy transfer behavior or structural changes, suggesting a different underlying mechanism. As mentioned above, Cr^{3+} and Cr^{4+} can coexist in the LZNO:Cr system due to the matching of the radius and valence state. Therefore, our initial focus was on observing the changes in the Cr valence state in the system before and after Er^{3+} doping. As shown in Fig. 5a and b, the high-resolution XPS spectra of the Cr 2p doublet in LZNO:0.01Cr^{3+} before and after Er^{3+} doping were analyzed. Four Gaussian components can be resolved in the two peaks of Cr. Specifically, the peaks at 586.17 and 577.65 eV are attributed to Cr $2p_{1/2}$ and Cr $2p_{3/2}$ components related to Cr^{4+} and they can be used to determine the Cr^{4+}/Cr^{3+} ratio. Obviously, the XPS peaks at 585.07and 575.58 eV are attributed to the Cr $2p_{1/2}$ and Cr $2p_{3/2}$ of Cr^{3+}.

It is found that, on co-doping with Er^{3+}, the peak area associated with Cr^{4+} is notably decreased and the peak area related to Cr^{3+} is significantly increased. This observation contrasts with the behavior of the LZNO phosphor doped solely with Cr^{3+}. It is evident that the addition of Er^{3+} effectively enhances the valence state transition from Cr^{4+} to Cr^{3+} in the LZNO system. Fig. S3b† shows the band gap variation of LZNO after Er^{3+} co-doping. Compared to Cr^{3+} single doping, 1.4% Er^{3+} co-doping resulted in a decrease in the band gap of LZNO from 2.62 eV to 2.45 eV. According to Fig. S1,† Er^{3+} doping will form impurity energy levels near the bottom of the conduction band in the LZNO host, thereby reducing the bandgap width. Moreover, due to Er^{3+} co-doping, it promotes the conversion of Cr^{4+} to Cr^{3+} in the system. Therefore, the change in the valence state of Cr leads to the broadening of the Cr^{3+} impurity energy level, as shown in Fig. S1c,† ultimately resulting in a decrease in the bandgap width. The decrease in the bandgap is consistent with the behavior of Cr^{3+} single doping, which may indicate that the concentration of Cr^{3+} ions in the system indeed increased.

Furthermore, to clarify the specific impact of Er^{3+} on promoting the conversion of Cr^{4+} to Cr^{3+}, the change in charge density after Er^{3+} doping to LZNO:Cr was calculated. As

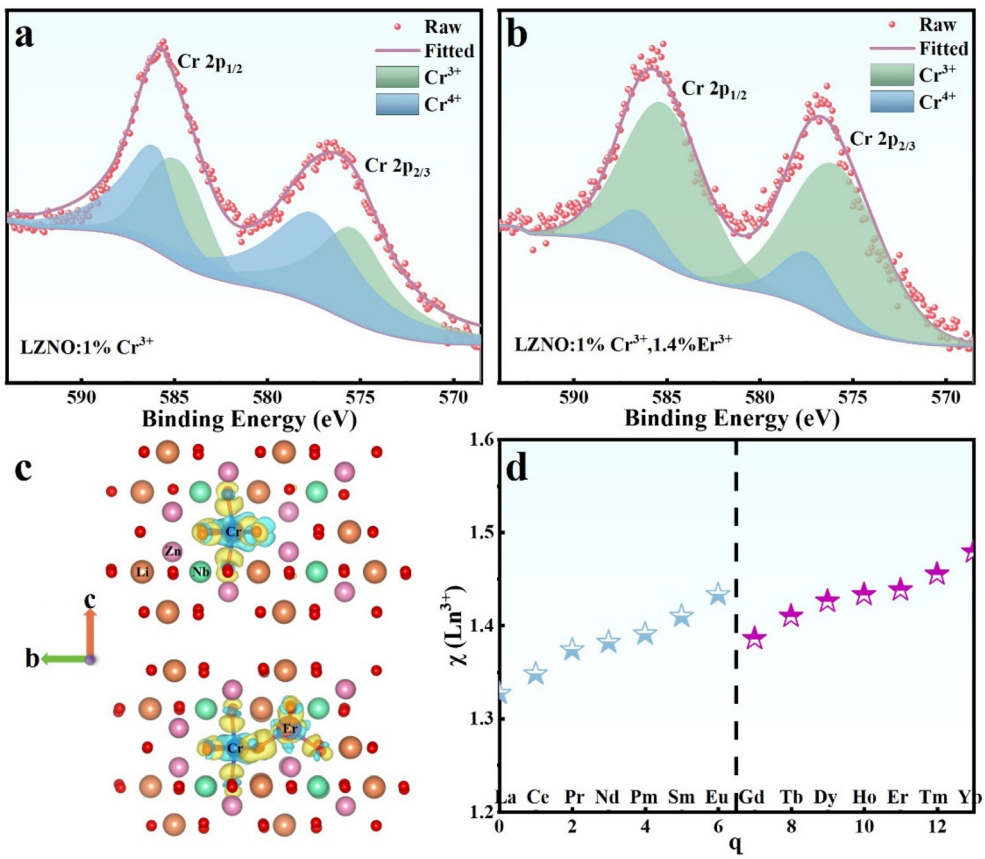

Fig. 5 (a) and (b) High-resolution Cr 2p XPS core energy level spectra of LZNO:0.01Cr^{3+} and LZNO:0.01Cr^{3+},0.014%Er^{3+}. (c) Deformation of the charge density comparison of Er^{3+}-doped LZNO:Cr before and after doping. (d) The variation pattern of the optical electronegativity of trivalent lanthanide ions with the number of 4f orbital electrons.

depicted in Fig. 5c, Cr^{3+} tends to shift electrons towards the surrounding O^{2-} anions. However, when Er^{3+} replaces the Zn^{2+} cation, Er^{3+} significantly redistributes the charge density around Cr and this results in an increase in its electron cloud, indicating that Cr^{4+} in the system will gain electrons and transform into Cr^{3+}. Therefore, we can conclude that the underlying mechanism of doping Er^{3+} that promotes the conversion of Cr^{4+} to Cr^{3+} is mainly through charge compensation. Then, a model is proposed that the heterotopic and heterovalent doping of Er^{3+} leads to defect charge compensation. This process can be explained by the following equation:

$$Cr_2O_3 \xrightarrow{Nb_2O_5} 2Cr''_{Nb} + 2V_O^{\cdot\cdot} + O_o^x \quad (5)$$

$$V_O^{\cdot\cdot} \rightarrow 2h^+ + O_o^x \quad (6)$$

$$Cr^{3+} + h^+ \rightarrow Cr^{4+} \quad (7)$$

$$Er_2O_3 \xrightarrow{2ZnO} 2Er_{Zn}^{\cdot} + V''_{Zn} + 3O_O^x \quad (8)$$

$$Er_2O_3 \xrightarrow{2ZnO} 2Er_{Zn}^{\cdot} + O''_i + 2O_o^x \quad (9)$$

$$V''_{Zn} \rightarrow 2e^+ + V_{Zn}^x \quad (10)$$

$$O''_i \rightarrow 2e^+ + O_o^x \quad (11)$$

$$Cr^{4+} + h^+ \rightarrow Cr^{3+} \quad (12)$$

When Cr^{3+} is doped into the LZNO host at high temperature (1100 °C), Cr^{3+} replaces Nb^{5+} to form Cr''_{Nb} defects because of valence mismatch. At the same time, to maintain charge balance, an equal amount of $V_O^{\cdot\cdot}$ is formed (eqn (5)). Positive charges in oxygen vacancies can be released under thermal disturbance, causing Cr^{3+} to self-oxidize to Cr^{4+} (eqn (6) and (7)). Similarly, when Er^{3+} is introduced to replace Zn^{2+}, negative zinc vacancy defects or interstitial oxygen defects will be generated to balance the charge (eqn (8) and (9)). Afterwards, electrons in these negatively charged defects can be released through thermal stimulation (eqn (10) and (11)). Due to the appropriate electronegativity of Er^{3+}, the constructed defect positions are suitable to form efficient electron transfer channels with Cr^{4+} within adjacent Nb^{5+} sites, ultimately allowing Cr^{4+} to capture electrons and reduce to Cr^{3+} (eqn (12)). Fig. S14a, b and c† show the high-resolution XPS spectra of the Zn 2p and O 1s core energy levels of LZNO:1% Cr^{3+} before and after Er^{3+} compensation. The diminished Zn signal, indicating an increase in Zn vacancies,[51] and the increased interstitial oxygen signal (chemically adsorbed oxygen peaks at 532 eV with adsorbed states that can be molecular, atomic, or interstitial oxygen[52–55]) in Er^{3+}-doped phosphors provide reliable evidence for our model.

The schematic diagram of the defect charge compensation mechanism model for Er^{3+} heterotopic and heterovalent doping is depicted in Fig. 6, and it can help us to vividly understand the valence conversion process of Cr ions. In the depicted scene, a mischievous demon is using fireball magic to attack Cr^{3+} ions. This process occurs during high-temperature sintering, where O_2 provides Cr^{3+} ions with positive charges to facilitate the formation of Cr^{4+}. In order to effectively suppress the transformation process of Cr ions, we introduced Er^{3+} ions into the Zn^{2+} sites. This action is akin to embedding an energetic magic stone in the core defense center, enabling the release of lightning magic through its own mechanism (zinc vacancy) and attracting elf fairies (inter-

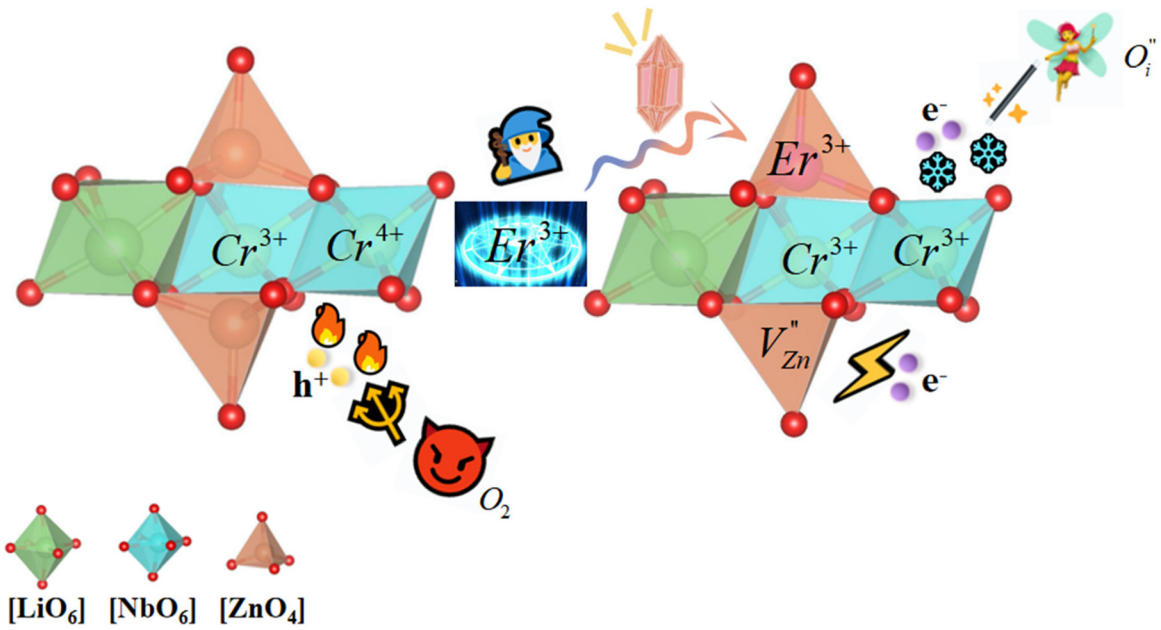

Fig. 6 Schematic diagram of the Cr valence-converting mechanism model *via* defect charge compensation for Er^{3+} heterotopic and heterovalent doping.

stitial oxygen) capable of employing frost magic. Together, these measures safeguard Cr^{3+} ions from the fireball assaults of the mischievous demon.

In order to confirm the reliability and universality of the proposed strategy, namely, the valence conversion of Cr^{4+} to Cr^{3+} induced by co-doped lanthanum ions of appropriate electronegativity, the relationship between the electronegativity of trivalent rare earth ions and the NIR luminescence of Cr^{3+} ions is further investigated. Fig. 5d shows the variation of the optical electronegativity of trivalent lanthanide ions with the number of 4f orbital electrons. As shown in Fig. S15,† besides Er^{3+}, both Dy^{3+} and Tm^{3+} can boost the NIR luminescence of Cr^{3+}. However, Nd^{3+} co-doping decreases the luminescence of Cr^{3+} ions. We proposed that this may be attributed to the variation in electronegativity among different rare earth ions, resulting in different defect constructions and charge compensation abilities. The electronegativity values of Dy^{3+}, Er^{3+}, and Tm^{3+} are very similar and the number of 4f electrons is also close. Although the electronegativity of Nd^{3+} is similar to that of Dy^{3+}, Er^{3+}, and Tm^{3+}, the difference in the number of 4f electrons is too large. Electronegativity indicates the ion's ability to attract electrons, while the variation in the number of 4f electrons indicates the difference in the chemical stability of lanthanide ions. Based on the above analysis, we predict that when Eu^{3+}/Yb^{3+} is doped into LZNO, the ion will not stabilize the Cr^{3+} ion due to partial/full 4f orbitals, as it is not possible to construct suitable defects to effectively compensate for electrons to Cr^{4+}. The luminescence quenching of Cr^{3+}, as shown in Fig. S16,† indeed proves our idea. In summary, the fundamental reason for co-doping trivalent rare earth ions to facilitate the conversion of Cr^{4+} to Cr^{3+} is closely linked to the electronegativity values of the lanthanide ions and the number of their 4f electrons.

3.6 Performance of NIR pc-LEDs

Finally, the actual application of the $LiZn(Er)NbO_4:Cr^{3+}$ phosphor was evaluated. Fig. 7a shows the NIR pc-LED device prototype fabricated by combining the as-prepared optimal $LiZn_{0.986}Er_{0.014}NbO_4:0.01Cr^{3+}$ phosphor and a 470 nm blue InGaN chip. Fig. 7b shows the electroluminescence (EL) spectra of the NIR pc-LED device under different forward bias currents (20–280 mA), while the NIR output power and photoelectric efficiency as a function of current are shown in Fig. S17.† With the increase in driving current, the NIR output power increased gradually from 0.21 to 1.66 mW, while the NIR photoelectric conversion efficiency decreased gradually from 0.41% to 0.21%. The continuous decrease in the current-dependent photoelectric efficiency may be attributed to the

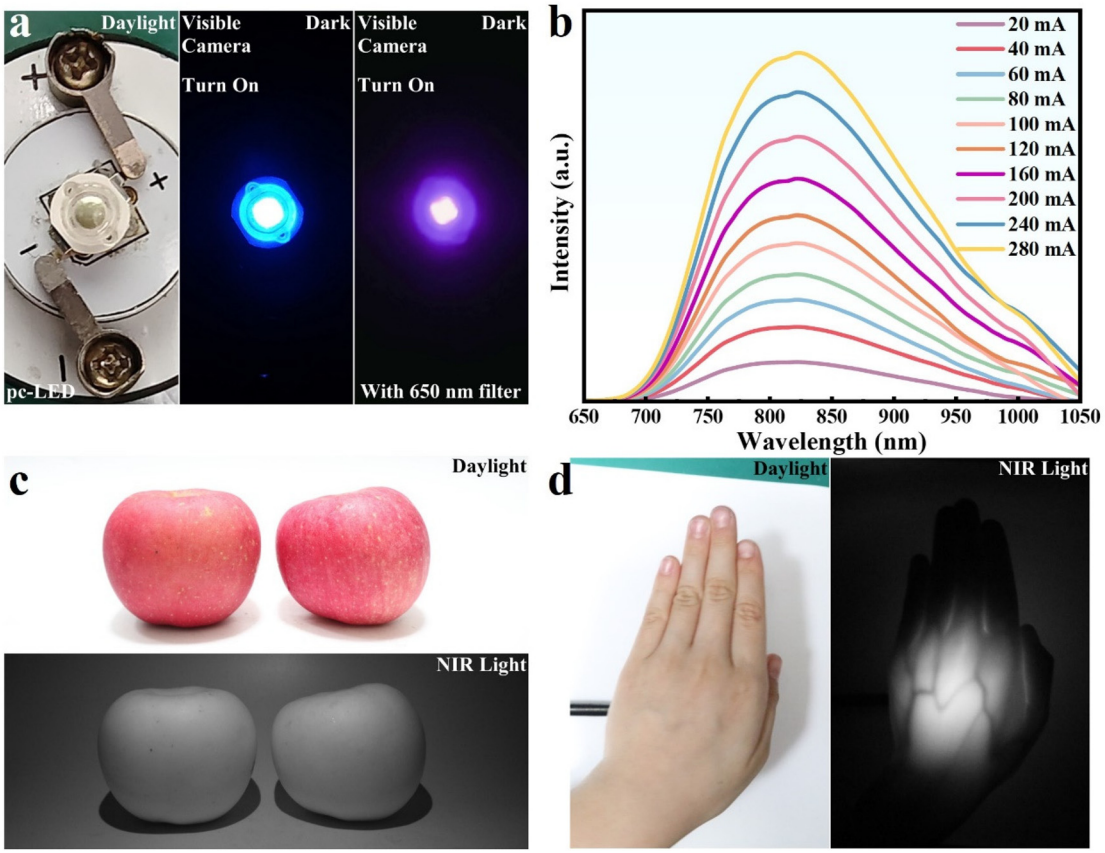

Fig. 7 (a) Working and nonworking states of the LED device. (b) Electroluminescence spectra of the prepared NIR pc-LED device that combines a 470 nm InGaN blue LED chip with the $LZNO:0.01Cr^{3+},0.014Er^{3+}$ NIR phosphor under a forward bias of 20–280 mA. Photographs of (c) an apple and (d) the palm captured under daylight using a visible light camera and under NIR pc-LED light using an NIR camera.

low absorption of the phosphor and thermal quenching resulting from the high-temperature working environment. Under strong currents, an apple can be clearly captured by an NIR camera under the light of the NIR pc-LEDs, as shown in Fig. 7c. Fig. 7d shows the particular use of our NIR phosphor in imaging a biological object. Placing the palm in front of the NIR pc-LEDs enabled the light to pass through easily, capturing the detailed blood vessel distribution. Under visible light, an ordinary camera was unable to reveal any clear details. While its photoelectric conversion efficiency properties still require improvement, these findings still emphasize the potential for real-world applications in night-vision and bio-tissue imaging technology.

4 Conclusion

In summary, according to the possible standards (1. high valence state; 2. large radius; and 3. low symmetry) proposed for achieving long-wavelength broadband emission of Cr ions in spinel-type crystals, we have successfully developed novel Cr-activated $LiZnNbO_4$ spinel phosphors with excellent long-wavelength NIR emission performance. Under the excitation of 468 nm blue light, LZNO:Cr^{3+} shows an ultra-wide and long-wavelength NIR emission at 800 nm and the designed $LiZnNbO_4$:Cr^{3+} was comprehensively investigated. In addition, a compensation strategy for defect charges involving the heterotopic doping of trivalent rare earth ions has been implemented to enhance the NIR luminescence of Cr^{3+} ions for the first time, which is closely linked to the electronegativity of lanthanide ions and the number of 4f electrons. Experimental evidence indicates that this strategy effectively promotes the valence state transformation of Cr^{4+} to Cr^{3+} in the LZNO:Cr^{3+} system, where 1.4%Er^{3+} co-doping increases the IQE from 8.3% to 17.8%. Finally, the LiZn(Er)NbO_4:Cr^{3+} phosphor was incorporated into a prototype NIR pc-LED device to demonstrate its practical application. This study not only broadens the range of spinel NIR luminescent materials activated by Cr^{3+}, but also explores the inherent relationship between rare earth ion heterotopic doping and Cr valence conversion. The design principles of Cr^{3+}-activated long-wavelength spinel phosphors and the NIR emission enhancement strategy proposed in this study may offer a roadmap for the efficient creation of long-wavelength NIR emitting phosphors activated by Cr^{3+}, and also presents a new approach for enhancing the luminescence efficiency.

Author contributions

Wen Song: conceptualization, methodology, data curation, and writing – original draft. Kaiwen Zhang: software and investigation. Xiaoyi Dong: data curation and resources. Liang Xu: data curation and resources. Yongjin Li, Rui Hu, and Zhiguo Song: project administration, funding acquisition, writing – review and editing, and supervision. Zhaoyi Yin: data curation and resources. Zhengwen Yang: data curation and resources. Jianbei Qiu: data curation and resources.

Data availability

All data supporting the findings of this study are available within the paper and its ESI.†

Conflicts of interest

The authors declare no competing interests.

Acknowledgements

This work was supported by the National Natural Science Foundation of China (No. 12264023), the National Natural Science Foundation of High and Foreign Experts Introduction Plan (No. G2022039008L), the Yunnan Major Scientific and Technological Projects (No. 202202AG050016), the Yunnan Fundamental Research Projects (No. 202301AT070459), the Analysis and Testing Foundation of Kunming University of Science and Technology (No. 2021T20200124) and the Yunnan Xing Dian Youth Talent Support Program (No. XDYC-QNRC-2022-0591). We also thank the Shiyanjia Lab (**https://www.shiyanjia.com**) for the XRD and XPS analyses and the Shenzhen Shuidi Scientific Research Service Co., Ltd for the testing of the PLQYs and NIR pc-LEDs.

References

1 A. T. Eggebrecht, S. L. Ferradal, A. Robichaux-Viehoever, M. S. Hassanpour, H. Dehghani, A. Z. Snyder, T. Hershey and J. P. Culver, Mapping distributed brain function and networks with diffuse optical tomography, *Nat. Photonics*, 2014, **8**, 448–454.

2 K. T. Ly, R. W. Chen-Cheng, H. W. Lin, Y. J. Shiau, S. H. Liu, P. T. Chou, C. S. Tsao, Y. C. Huang and Y. Chi, Near-infrared organic light-emitting diodes with very high external quantum efficiency and radiance, *Nat. Photonics*, 2017, **11**, 63–68.

3 G. C. Liu, M. S. Molokeev and Z. G. Xia, Structural Rigidity Control toward Cr^{3+}-Based Broadband Near-Infrared Luminescence with Enhanced Thermal Stability, *Chem. Mater.*, 2022, **34**, 1376–1384.

4 L. Huang, Z. J. Li, Y. Zhao, J. Y. Yang, Y. C. Yang, A. I. Pendharkar, Y. W. Zhang, S. Kelmar, L. Y. Chen, W. T. Wu, J. Z. Zhao and G. Han, Enhancing Photodynamic Therapy through Resonance Energy Transfer Constructed Near-Infrared Photosensitized Nanoparticles, *Adv. Mater.*, 2017, **29**, 7.

5 Q. Y. Shao, H. Ding, L. Q. Yao, J. F. Xu, C. Liang and J. Q. Jiang, Photoluminescence properties of a $ScBO_3$:Cr^{3+}

phosphor and its applications for broadband near-infrared LEDs, *RSC Adv.*, 2018, **8**, 12035–12042.

6 W. T. Huang, C. L. Cheng, Z. Bao, C. W. Yang, K. M. Lu, C. Y. Kang, C. M. Lin and R. S. Liu, Broadband Cr^{3+}, Sn^{4+}-Doped Oxide Nanophosphors for Infrared Mini Light-Emitting Diodes, *Angew. Chem., Int. Ed.*, 2019, **58**, 2069–2072.

7 Z. W. Pan, Y. Y. Lu and F. Liu, Sunlight-activated long-persistent luminescence in the near-infrared from Cr^{3+}-doped zinc gallogermanates, *Nat. Mater.*, 2012, **11**, 58–63.

8 L. F. Yuan, Y. H. Jin, H. Y. Wu, K. Y. Deng, B. Y. Qu, L. Chen, Y. H. Hu and R. S. Liu, Ni^{2+}-Doped Garnet Solid-Solution Phosphor-Converted Broadband Shortwave Infrared Light-Emitting Diodes toward Spectroscopy Application, *ACS Appl. Mater. Interfaces*, 2022, **14**, 4265–4275.

9 Z. Liao, H. Xu, W. Zhao, H. Yang, J. Zhong, H. Zhang, Z. Nie and Z.-K. Zhou, Energy transfer from Mn^{4+} to Mn^{5+} and near infrared emission with wide excitation band in $Ca_{14}Zn_6Ga_{10}O_{35}$:Mn phosphors, *Chem. Eng. J.*, 2020, **395**, 125060.

10 X. Z. Chen, Y. Li, K. Huang, L. Huang, X. M. Tian, H. F. Dong, R. Kang, Y. H. Hu, J. M. Nie, J. R. Qiu and G. Han, Trap Energy Upconversion-Like Near-Infrared to Near-Infrared Light Rejuvenateable Persistent Luminescence, *Adv. Mater.*, 2021, **33**, 7.

11 F. Ren, L. H. Ding, H. H. Liu, Q. Huang, H. Zhang, L. J. Zhang, J. F. Zeng, Q. Sun, Z. Li and M. Y. Gao, Ultrasmall nanocluster mediated synthesis of Nd^{3+}-doped core-shell nanocrystals with emission in the second near-infrared window for multimodal imaging of tumor vasculature, *Biomaterials*, 2018, **175**, 30–43.

12 J. W. Qiao, G. J. Zhou, Y. Y. Zhou, Q. Y. Zhang and Z. G. Xia, Divalent europium-doped near-infrared-emitting phosphor for light-emitting diodes, *Nat. Commun.*, 2019, **10**, 7.

13 P. Kaithrikkovil Varriam and S. Ganesanpotti, Harnessing the Dual–Mode Luminescence of Er/Yb Co–Doped $SrLaLiTeO_6$ Double Perovskite Phosphors for Remarkably Wide Range Temperature Sensing and NIR pc–LEDs, *Laser Photonics Rev.*, 2024, DOI: **10.1002/lpor.202400245**.

14 P. P. Dang, Y. Wei, D. J. Liu, G. G. Li and J. Lin, Recent Advances in Chromium-Doped Near-Infrared Luminescent Materials: Fundamentals, Optimization Strategies, and Applications, *Adv. Opt. Mater.*, 2023, **11**, 27.

15 S. H. Miao, Y. J. Liang, Y. Zhang, D. X. Chen and X. J. Wang, Broadband Short-Wave Infrared Light-Emitting Diodes Based on Cr^{3+}-Doped $LiScGeO_4$ Phosphor, *ACS Appl. Mater. Interfaces*, 2021, **13**, 36011–36019.

16 M. U. Dumesso, W. G. Xiao, G. J. Zheng, E. T. Basore, M. X. Tang, X. F. Liu and J. R. Qiu, Efficient, Stable, and Ultra-Broadband Near-Infrared Garnet Phosphors for Miniaturized Optical Applications, *Adv. Opt. Mater.*, 2022, **10**, 8.

17 X. K. Zou, X. J. Wang, H. R. Zhang, Y. Y. Kang, X. Yang, X. J. Zhang, M. S. Molokeev and B. F. Lei, A highly efficient and suitable spectral profile Cr^{3+}-doped garnet near-infrared emitting phosphor for regulating photomorphogenesis of plants, *Chem. Eng. J.*, 2022, **428**, 9.

18 T. Y. Liu, H. Cai, N. Mao, Z. Song and Q. L. Liu, Efficient near-infrared pyroxene phosphor $LiInGe_2O_6$:Cr^{3+} for NIR spectroscopy application, *J. Am. Ceram. Soc.*, 2021, **104**, 4577–4584.

19 X. X. Xu, Q. Y. Shao, L. Q. Yao, Y. Dong and J. Q. Jiang, Highly efficient and thermally stable Cr^{3+}-activated silicate phosphors for broadband near-infrared LED applications, *Chem. Eng. J.*, 2020, **383**, 8.

20 Q. M. Lin, Q. Wang, M. Liao, M. X. Xiong, X. Feng, X. Zhang, H. F. Dong, D. Y. Zhu, F. G. Wu and Z. F. Mu, Trivalent Chromium Ions Doped Fluorides with Both Broad Emission Bandwidth and Excellent Luminescence Thermal Stability, *ACS Appl. Mater. Interfaces*, 2021, **13**, 18274–18282.

21 T. Q. Zhao, R. Abdurahman, R. Aiwaili, S. Q. Wu and X. B. Yin, Spinel-type persistent luminescence nanoparticles: From mechanisms, compositions to applications, *Coord. Chem. Rev.*, 2023, **488**, 25.

22 W. T. Huang, K. C. Chen, M. H. Huang and R. S. Liu, Tunable Spinel Structure Phosphors: Dynamic Change in Near-Infrared Windows and Their Applications, *Adv. Opt. Mater.*, 2023, 22, DOI: **10.1002/adom.202301166**.

23 H. J. Jiang, L. Y. Chen, G. J. Zheng, Z. H. Luo, X. H. Wu, Z. H. Liu, R. Y. Li, Y. F. Liu, P. Sun and J. Jiang, Ultra-Efficient GAGG:Cr^{3+} Ceramic Phosphor-Converted Laser Diode: A Promising High-Power Compact Near-Infrared Light Source Enabling Clear Imaging, *Adv. Opt. Mater.*, 2022, **10**, 8.

24 L. P. Jiang, X. Jiang, C. X. Wang, P. Liu, Y. Zhang, G. C. Lv, T. Lookman and Y. J. Su, Rapid Discovery of Efficient Long-Wavelength Emission Garnet:Cr NIR Phosphors via Multi-Objective Optimization, *ACS Appl. Mater. Interfaces*, 2022, **14**, 52124–52133.

25 V. Rajendran, M. H. Fang, G. N. De Guzman, T. Lesniewski, S. Mahlik, M. Grinberg, G. Leniec, S. M. Kaczmarek, Y. S. Lin, K. M. Lu, C. M. Lin, H. Chang, S. F. Hu and R. S. Liu, Super Broadband Near-Infrared Phosphors with High Radiant Flux as Future Light Sources for Spectroscopy Applications, *ACS Energy Lett.*, 2018, **3**, 2679–2684.

26 V. Rajendran, W. T. Huang, K. C. Chen, H. Chang and R. S. Liu, Energy-saving chromium-activated garnet-structured phosphor-converted near-infrared light-emitting diodes, *J. Mater. Chem. C*, 2022, **10**, 14367–14378.

27 J. Q. Fan, W. Y. Zhou, J. L. Zhang, P. C. Chen, Q. Pang, L. Y. Zhou, C. Y. Zhou and X. G. Zhang, A novel efficient broadband near-infrared phosphor $LiGaGe_2O_6$:Cr^{3+} with EQE enhancement and spectral tuning by Sc^{3+}-Ga^{3+} substitution for NIR pc-LED application, *Inorg. Chem. Front.*, 2023, **10**, 511–521.

28 F. Y. Zhao, H. Cai, Z. Song and Q. L. Liu, Structural Confinement for Cr^{3+} Activators toward Efficient Near-Infrared Phosphors with Suppressed Concentration Quenching, *Chem. Mater.*, 2021, **33**, 3621–3630.

29 Y. Wang, Z. Wang, G. Wei, Y. Yang, S. He, J. Li, Y. Shi, R. Li, J. Zhang and P. Li, Ultra-Broadband and high efficiency Near-Infrared $Gd_3Zn_xGa_{5-2x}Ge_xO12:Cr^{3+}$ (x = 0–2.0) garnet phosphors via crystal field engineering, *Chem. Eng. J.*, 2022, **437**, 135346.
30 M. Ferriol and S. Lecocq, Structural characterization of $ZnLiNbO_4$, *Eur. J. Solid State Inorg. Chem.*, 1998, **35**, 707–714.
31 H. Cai, H. Chen, H. Zhou, J. Zhao, Z. Song and Q. L. Liu, Controlling Cr^{3+}/Cr^{4+} concentration in single-phase host toward tailored super-broad near-infrared luminescence for multifunctional applications, *Mater. Today Chem.*, 2021, **22**, 7.
32 Z. W. Jia, C. X. Yuan, Y. F. Liu, X. J. Wang, P. Sun, L. Wang, H. C. Jiang and J. Jiang, Strategies to approach high performance in Cr^{3+}-doped phosphors for high-power NIR-LED light sources, *Light: Sci. Appl.*, 2020, **9**, 9.
33 T. Y. Gao, W. D. Zhuang, R. H. Liu, Y. H. Liu, C. P. Yan, J. Tian, G. Chen, X. Chen, Y. H. Zheng and L. G. Wang, Site occupancy and enhanced luminescence of broadband NIR gallogermanate phosphors by energy transfer, *J. Am. Ceram. Soc.*, 2020, **103**, 202–213.
34 G. Merkininkaite, A. Zabiliute-Karaliune, T. Jüstel, V. Klimkevicius, S. Sakirzanovas and A. Katelnikovas, $Ce^{3+} \rightarrow Cr^{3+}$ energy transfer in $Y_3Al_3MgSiO_{12}$ garnet host and application in horticultural lighting, *Ceram. Int.*, 2023, **49**, 16796–16808.
35 S. C. Lal, I. N. Jawahar and S. Ganesanpotti, Enhancing the inherent NIR photoluminescence in $SrLaLiTeO_6$ through Cr^{3+}-Yb^{3+} co-substitution for high performance pc-LEDs, *Dalton Trans.*, 2024, **53**, 1230–1244.
36 J. Hafner, *Ab initio* simulations of materials using VASP:: Density-functional theory and beyond, *J. Comput. Chem.*, 2008, **29**, 2044–2078.
37 J. Heyd, G. E. Scuseria and M. Ernzerhof, Hybrid functionals based on a screened Coulomb potential, *J. Chem. Phys.*, 2003, **118**, 8207–8215.
38 N. W. Ashcroft and N. D. Mermin, *Solid State Physics*, Cengage Learning Press, 1976.
39 G. B. M. Melo, S. S. Pedro, A. López, G. K. B. Costa and L. P. Sosman, Unexpected photoluminescence from Mn^{2+} in $LiZnNbO_4$, *Opt. Mater.*, 2020, **99**, 5.
40 S. Adachi, Photoluminescence Properties of Cr^{3+}-Activated Oxide Phosphors, *ECS J. Solid State Sci. Technol.*, 2021, **10**, 20.
41 P. Makula, M. Pacia and W. Macyk, How To Correctly Determine the Band Gap Energy of Modified Semiconductor Photocatalysts Based on UV-Vis Spectra, *J. Phys. Chem. Lett.*, 2018, **9**, 6814–6817.
42 R. G. J. Tauc and A. Vancu, Optical Properties and Electronic Structure of Amorphous Germanium, *Phys. Status Solidi*, 1996, 627–637.
43 V. V. Atuchin, L. I. Isaenko, V. G. Kesler, Z. S. Lin, M. S. Molokeev, A. P. Yelisseyev and S. A. Zhurkov, Exploration on anion ordering, optical properties and electronic structure in $K_3WO_3F_3$ elpasolite, *J. Solid State Chem.*, 2012, **187**, 159–164.
44 Z. Xia, Y. Zhang, M. S. Molokeev and V. V. Atuchin, Structural and Luminescence Properties of Yellow-Emitting $NaScSi_2O_6:Eu^{2+}$ Phosphors: Eu^{2+} Site Preference Analysis and Generation of Red Emission by Codoping Mn^{2+} for White-Light-Emitting Diode Applications, *J. Phys. Chem. C*, 2013, **117**, 20847–20854.
45 H. Ji, Z. Huang, Z. Xia, M. S. Molokeev, X. Jiang, Z. Lin and V. V. Atuchin, Comparative investigations of the crystal structure and photoluminescence property of eulytite-type $Ba_3Eu(PO_4)_3$and $Sr_3Eu(PO_4)_3$, *Dalton Trans.*, 2015, **44**, 7679–7686.
46 F. Y. Zhao, Z. Song and Q. L. Liu, Advances in Chromium-Activated Phosphors for Near-Infrared Light Sources, *Laser Photonics Rev.*, 2022, **16**, 42.
47 B. Bai, P. P. Dang, D. Y. Huang, H. Z. Lian and J. Lin, Broadband Near-Infrared Emitting $Ca_2LuScGa_2Ge_2O_{12}:Cr^{3+}$ Phosphors: Luminescence Properties and Application in Light-Emitting Diodes, *Inorg. Chem.*, 2020, **59**, 13481–13488.
48 G. C. Liu, M. S. Molokeev, B. F. Lei and Z. G. Xia, Two-site Cr^{3+} occupation in the $MgTa_2O_6:Cr^{3+}$ phosphor toward broad-band near-infrared emission for vessel visualization, *J. Mater. Chem. C*, 2020, **8**, 9322–9328.
49 J. Y. Zhong, Y. Zhuo, F. Du, H. S. Zhang, W. R. Zhao, S. H. You and J. Brgoch, Efficient Broadband Near-Infrared Emission in the $GaTaO_4:Cr^{3+}$ Phosphor, *Adv. Opt. Mater.*, 2022, **10**, 8.
50 B. Struve and G. Huber, The effect of the crystal field strength on the optical spectra of Cr^{3+} in gallium garnet laser crystals, *Appl. Phys. B: Photophys. Laser Chem.*, 1985, 195–201.
51 V. V. Atuchin, E. N. Galashov, O. Y. Khyzhun, A. S. Kozhukhov, L. D. Pokrovsky and V. N. Shlegel, Structural and Electronic Properties of $ZnWO_4$ (010) Cleaved Surface, *Cryst. Growth Des.*, 2011, **11**, 2479–2484.
52 V. V. Atuchin, J. C. Grivel, A. S. Korotkov and Z. Zhang, Electronic parameters of $Sr_2Nb_2O_7$ and chemical bonding, *J. Solid State Chem.*, 2008, **181**, 1285–1291.
53 V. V. Atuchin, D. A. Vinnik, T. A. Gavrilova, S. A. Gudkova, L. I. Isaenko, X. Jiang, L. D. Pokrovsky, I. P. Prosvirin, L. S. Mashkovtseva and Z. Lin, Flux Crystal Growth and the Electronic Structure of $BaFe_{12}O_{19}$ Hexaferrite, *J. Phys. Chem. C*, 2016, **120**, 5114–5123.
54 Z. Xing, P. Li, D. Dai, X. Li, C. Liu, L. Zhang and Z. Wang, Self-Luminescence of Perovskite-Like $LaSrGaO_4$ via Intrinsic Defects and Anomalous Luminescence Analysis of $LaSrGaO_4:Mn^{2+}$, *Inorg. Chem.*, 2019, **58**, 4869–4879.
55 X. Kang, W. Lü, Z. Zhu and Q. Pan, Multiple defects induced near-infrared self-luminescence of (Ca,Sr) $LaMgTaO_6$ double perovskite phosphor, *Ceram. Int.*, 2023, **49**, 32719–32726.

